Effective Classification of Multi-class Brain Cancers using feature-optimized Convolutional Neural Network

[1]Deepak V.K, [2]Sarath. R

[1]Research Scholar, Department of Electronics & Communication, Noorul Islam Centre for Higher Education, Thuckalay, Kumaracoil, Tamilnadu.

deepakvk2@gmail.com

[2]Assistant Professor, Department of Electronics &Instrumentation, Noorul Islam Centre for Higher Education, Thuckalay, Kumaracoil, Tamilnadu.

sarathraveendran@gmail.com

ABSTRACT

Recently, deep learning has gained a lot of attention as a modern area in machine learning. It is seen to be an effective machine-learning technique for resolving a wide range of challenging issues in numerous applications. The prevention of brain cancer, one of the main reasons for death for women, has been the subject of significant financial investment in screening programs. Without numerous systematic readings, computer-assisted detection methods created to enhance diagnostics have not yet appreciably altered performance measurements. As a result of deep learning, automated image processing techniques could potentially help diagnose brain cancer. The fuzzy system hybrid deformable model, super pixel-based adaptive clustering, extraction of features tool, and a Tetrolet Transform (TT) developed from Harish Hawks Optimization (HHO) were used to excellent effect in all performance stages. Outcomes from experiments show ResNet CNN processed MRI images with a high degree of precision.

Keywords: Hybrid deformable model with the fuzzy method and superpixels adaptive fuzzy clustering, Convolutional Neural Network, Tetrolet transform, Harish Hawks Optimization

198

1. INTRODUCTION

The body's growth and cell division are uncontrolled and unnatural in cancer. The growth and division of unnatural cells in the brain tissue are referred to as brain tumor. There is no doubt that brain tumors are among the deadliest cancers despite their rarity. Magnetic Resonance Imaging (MRI) and Computed Tomography (CT) can be used to scan the structure of the brain. Diagnostic CT scans are less stressful than MRI scans. It is safe for the human body because there is no radiation. It is supported by a radio wave and a magnetic field[1]. On the other hand, human brain tumours are a major cause of death. A correct diagnosis of a tumor has a high survival chance. Strokes are typically

treated by doctors instead of tumors. The tumor must therefore be detected to be treated. If a brain tumor is detected early, the infected person's lifespan will increase [2]. Therefore, a technique that offers little user engagement, quick computation, and precise and reliable selected features is needed for medical image segmentation. Researchers offered many automated methods for recognizing and classifying brain tumors since it was feasible to scan and upload medical data to a computer. But over the past few decades, Support Vector Machines (SVM) and Neural Networks (NN) have become widely employed techniques to their success [3]. As deep networks get more effective, Deep Learning (DL) methods have been becoming increasingly popular recently. The most widely used image processing models at the moment are Convolutional Neural Networks (CNNs).

RELATED WORK

These pivotal developments have been noticed by the medical image analysis community. [4] Veeramuthu et al recommended employing a mix of machine learning and a review of the brain's structural characteristics to categorize brain images. The characteristics of an image can be extracted using a "Multi-Level Discrete Wavelet Transform". PNN-RBF training and classification are used to categorize the stages of a brain picture. Hybrid techniques were developed by Sanjeev et al.[5]. A Support Vector Machine (SVM) classifies brain tumors by removing features, using evolutionary algorithms to reduce the number of characteristics, and by using

Discrete Wavelet Transforms (DWT). Gopal et al.[6] have made attempts to improve the categorization of motor pictures using Feed-Forward Back-Propagation Neural Networks (FFBPNN). Artificial Neural Networks (ANNs), Fuzzy C-Means (FCMs), Support Vector Machines (SVMs), decision trees, K-Nearest Neighbors (KNNs), and Bayesian classification algorithms are just a few of the methods that can be used to classify medical pictures. Supervised learning procedures include ANNs, SVMs, and KNNs. Self-organizing maps and K-means clustering are examples of unsupervised learning for clustering data. It has taken a while for systems using handmade features to move to systems learning data features. In the past, several different techniques were used to learn features before AlexNet's breakthrough. Bengio et al[7] .'s in-depth examination of various methods is available. Many of these use dictionary methods, picture patch clustering, and main component analyses. After their investigation, Moosa et al.[8] trains CNNs end-to-end in a section headed Global Training of Deep Models. This survey focuses on these deep-rooted models and leaves out more traditional feature-learning techniques. In Ravi et al(2017)[9] .'s brief examination of deep learning in health informatics, the interpretation of medical images is discussed. According to Shen et al. (2017)[10], deep learning was used to analyze medical images. It indicates crucial regions of work.

Problem Statement

One of the main challenges to image segmentation and categorization is the lack of a standardized protocol that can be used for all kinds of images and scenarios. Even choosing the right approach for a specific image type might be challenging. Consequently, the segmentation and classification of images are not widely accepted. It continues to be a challenge for computer vision and image processing. The method neglected to take into account categorizing photos of distinct clinical disorders, types, and sickness conditions. There are many pure nodes in the system, which may lead to overfitting. We devised a deep learning approach to detect brain tumors automatically and evaluated their performance using brain MRI data.

The contribution of the proposed work

- To enhance the image, we used an innovative boosted adaptive anisotropic diffusion filter.
- Two steps are taken in segmentation. In the first step, the BSE (Brain Surface Extractor) method is used to separate the skull component from the MR brain image. To retrieve the tumor region from the brain segment after the tumor has been removed, an adaptive clustering method using a hybrid deformable model and fuzzy methods is used.
- Texture and the tetrolet transforms are used to obtain the features, which are then merged using the Harish Hawks optimization process.

- The recommended method aims to tell the CNN classifier apart between typical brain tumors and aberrant brain MRI images.

The methodology we suggest is robust and totally automatic. There is no need to know the qualities, characteristics, form, or model of the image before using it. The suggested approach is a highly accurate strategy for diagnosing brain tumors.

The paper is organized as follows: Part two contains examples of the pertinent work. Part three defines the specifics of the proposed methods, while part four describes the performance measures. The results of the experiment are described in part five. Part six discusses the conclusion and next work.

2. PROPOSED METHOD

The proposed approach differentiates and classifies the various stages of a brain tumor. First, the image must be pre-processed to remove noise. During segmentation, the brain is separated from the skull and the remaining elements of the image. Following the extraction of features, a process of choosing attributes from among them is performed. Figure 1 illustrates how the tumorous region was finally classified.

3.1 Pre-processing

Before any special processing goals, a series of initial processing processes are applied to the image in this step. It decreases noise and improves image accuracy. Brain images should be of the highest quality and with the least amount of noise possible because they are more sensitive than other medical imaging [10]. The two sub-stages listed below make up this phase:

- **De-noising:** Gaussian and Poisson noises usually alter MRI images[11]. Gaussian white noise is used in most de-noising techniques. A variety of methods are designed to get rid of Gaussian noise, including ones that preserve bilateral filter edges, total variance, and non-local means. An improved adaptive anisotrophic diffusion filter is used in this case. It is a non-linear filter with

-

good background noise removal capabilities. Following the denoising procedure, the image is enhanced using the histogram equalization method.

- **Skull removal:** Even though picture history typically doesn't provide any valuable knowledge, it slows down processing. Therefore, removing the past, the skull, the hair, the eyes, and any other characteristics that are unimportant reduces the amount of memory utilized and speeds up processing. The skull is removed using the BSE algorithm. For MRI images exclusively, the BSE algorithm is employed, removes anomalies from the image, finds the image's edges and carries out morphological erosion and brain isolation. Additionally, it masks the images and cleans the surface [12].
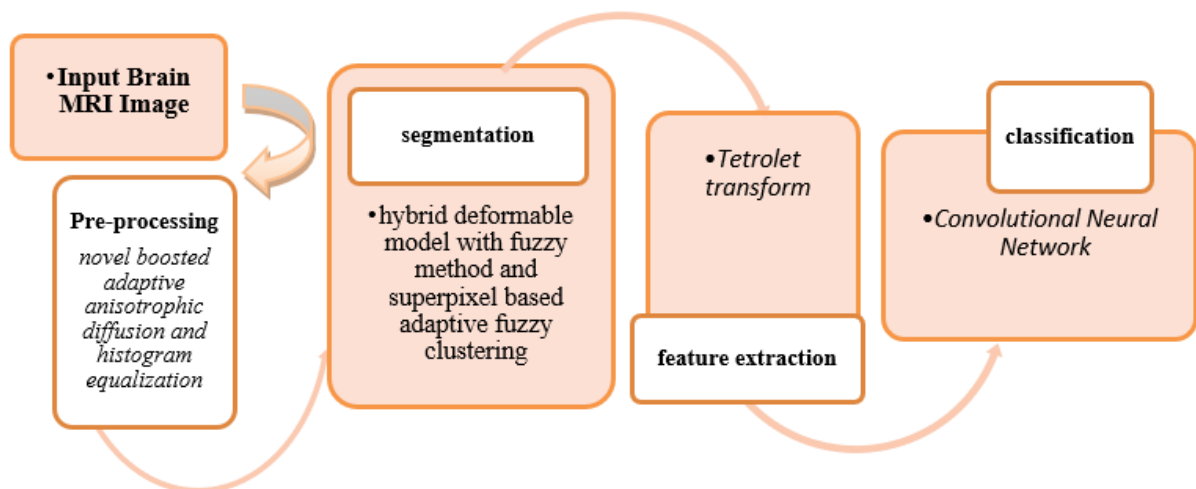
201

Figure1: General layout of the proposed work

3.2 Image Segmentation

Cerebrospinal Fluid (CSF), White Matter (WM), and grey matter are only a few examples of normal brain tissues that

can be distinguished from tumor tissues using the picture segmentation strategy in Magnetic Resonance Imaging (MRI) of the brain (GM). Due to its improved

effectiveness, the picture was split into five sections using a hybrid deformation model that makes use of a fuzzy reasoning method and hyper-sensor adaptable clusters.

A hybrid deformable model with a fuzzy method

In the areas of pattern detection and computer vision, deformable models have had huge success. The two main types of deformable models are explicit and implicit. Deformable structures were primarily intended for the segmentation of medical pictures and the reconstruction of shapes using volumetric knowledge, as was previously indicated. The majority of recent work on point cloud shape restoration uses static approaches [13]. The simple choices are the Delaunay triangulation or the Voronoi diagram. Deformable models are dynamic, 2D or 3D designs that adapt to both internal and external variables. For the form to remain smooth, internal forces are assessed. The curve or surface is transferred to the required position by applying external forces that are estimated from the photographs.

The most popular technique for segmenting images is the fuzzy algorithm since it keeps a lot more features than the hard segmentation technique and has a more reliable uncertain function. Dunn was the first to present the fuzzy C-means algorithm, and Bezdek later improved it. Each cluster has its own membership coefficient, which enables the test pixel to be part of multiple clusters with this method. This method is discussed in depth in [14] and results in a cluster centre with an optimization problem as well as a fuzzy partition matrix. The cluster centre evaluation and objective function are adjusted for every cycle when the difference between the two succeeding results is less than a predetermined threshold level. By minimizing the squared error optimization problem within the group sum[12], the FCM algorithm generates the ideal C partition as given below.

$$J_{FCM} = \sum_{k=1}^{n} \sum_{i=1}^{c} (v_{ik})^q \, d^2(X_k, V_i) \qquad (1)$$

where, $x = x_1, x_2, .., x_n \leq R$ shows the dataset, n denotes no. of data items, c represents clusters numbers $2 \leq c < n$, $v_{i,k}$ degree of membership of X_k in i^{th} cluster, q-weighting exponent of every fuzzy member, and v_i prototype of centre cluster i.

- **Superpixel based adaptive clustering**

In the proposed approach, images are divided into tiny, equal chunks. The propensity of a data collection to group its observations around a single significant component is frequently referred to as the Central Tendency Value (CTV). By using mean, median, and mode, the CTV of each block is computed, and the superpixel value for each block is then calculated.

A block's average value is measured as the average of all the pixel values within it. Let the letters B_1, B_2, B_3,..., and B_n stand in for the image I's blocks, with m denoting the number of blocks. Assuming that n is the

no. of pixels in the block, let's use P_1; P_2; P_3... P_n to denote the pixel intensity value.

$$M_i = \frac{1}{n}\sum_{j=1}^{n} p_j^i \qquad (2)$$

p_j^i will be the j pixel value of the ith block B_i in the given image I. The CTV was calculated using median med_i represents the median value of ith block B_i and evaluated using the steps given below.

1. Arrange the pixel values of ith block B_i of the given image I.

2. Then CT was measured using the median med_i is given in the Eqn. 36

$$med_i =$$

$$\begin{cases} \frac{1}{2}\left(p_i^{\frac{n}{2}} + p_i^{\frac{n}{2}+1}\right) & \text{if n mod2} = \\ p_i^{\frac{n}{2}} & \text{if n mod2} \neq 0 \\ = 0 \end{cases} \qquad (3)$$

here, n = 1; pixels nos of ith block B_i . $p_i^{\frac{n}{2}}$ is $(n/2)^{th}$ the pixel value of ith block B_i. $p_i^{\frac{n}{2}+1}$ is $\left(\frac{n}{2}+1\right)^{th}$ The pixel value of ith blocks B_i . $p_i^{\frac{n+1}{2}}$ is $\left(\frac{n+1}{2}\right)^{th}$ .Pixel value of ith blocks B_i and i = 1; 2..m, no. of blocks of the image.

Using mode AP I as the mode value for the ith block of image I, the most frequent pixel value p I is calculated as the CTV. The no. of blocks in the image is I = 1; 2,..., n, and m. Now, CTV-calculated superpixels from blocks are used to display the complete image. Spectral clustering is used to segment these superpixels. The next section defines data about the separation of the superpixels. The super image pixels of the picture's blocks are subjected to adaptive clustering. To produce superpixel tumors and superpixel tumors, superpixel segmentation is used. Compared to the existing algorithm, the suggested segmentation algorithm resolves all its drawbacks. Regardless of the original membership values, it consistently produces the same segmentation results. Since the impact of the picture intensity is minimal, the segmentation's precision is good. Furthermore, the proposed method algorithm requires much less calculation time because it uses straightforward, quick, and regular morphological processes.

3.3 . Feature extraction and reduction

The characteristics of the segmentation tumor are retrieved utilizing texture[17] and Tetrolet Transform (TT) [16] features after the Brain MR images have been divided into 5 sections. Because TT offers localized signal frequency information and employs cascaded high-pass and low-pass filter banks to features extracted hierarchically [13], it has the benefit of recovering the most significant characteristics in a variety of directions and scales.

- **Texture Features**

By detecting their frequency in a particular spatial region, an algorithm connects two pixels to an image. These relationships are used to create a Co-Occurrence Matrix (CCM), which is used to generate statistical metrics. Each point in the CCM matrix represents the frequency of how frequently that particular pixel was seen there. This method is employed by GLCM to assess its

203

performance. Despite the availability of numerous feature extraction, only four are employed in this study: energy, contrast, correlations, and homogeneity[14].

Energy

$$\sum_{i=0}^{G-1} \sum_{j=0}^{G-1} [p(i,j)]^2 \qquad (4)$$

$$Homogenity = -\sum_{i=0}^{G-1} p(i) \log_2 [p(i)] \qquad (5)$$

Correlation =

$$\sum_{i=0}^{G-1} \sum_{i=0}^{G-1} \frac{ij \, p(i,j) - \mu_x \mu_y}{\sigma_x \sigma_y} \qquad (6)$$

Contrast =

$$\sum_{i=0}^{G-1} \sum_{j=0}^{G-1} (i-j)p(i,j) \qquad (7)$$

Included in the characteristics of colour are mean, SD, skewness, kurtosis, and entropy. Entropy indicates how much image data is required to compress a given image. Through the use of a Colour Moment (CM) descriptor, these qualities are determined. The following table lists the equations' statistical properties (FOS):

$$Mean \, \mu = \sum_{i=0}^{G-1} i \, p(i) \qquad (8)$$

$$Variance \, \sigma^2 = \sum_{i=0}^{G-1} (i-\mu)^2 p(i) \qquad (9)$$

$$Skewness \, \mu_3 = \sigma^{-3} \sum_{i=0}^{G-1} (i-\mu)^3 p(i) \qquad (10)$$

$$Kurtosis \, \mu_4 = \sigma^{-4} \sum_{i=0}^{G-1} (i-\mu)^4 p(i) \qquad (11)$$

Entropy = H =

$$-\sum_{i=0}^{G-1} \sum_{j=0}^{G-1} p(i,j) \log_2 [p(i)] \qquad (12)$$

- **Tetrolet Transform (TT).**

The multi-scale tetrolet decomposition of the input noisy picture is then achieved by following the stages: 〚 g=[g(x,y)]〛 _(x,y=1)^N with 〚 N = 2〛 ^k, K∈N, whereas the tetromino covering c and the number of decomposition rates J are also produced. Starting with the input images, 〚 g=[g(x,y)]〛 _(x,y=1)^N. Then proceed and perform the computations listed below at the j-th level, where j=1.

1. Low-pass image is divided g^{j-1} into 4 ×4 blocks, $Q_{m,n}$ $m, = 1 \ldots \frac{N}{2^{j+1}}$.

2. In every block $Q_{m,n}$ the low-pass part for tetromino covering is evaluated by c

$$g^{j,(c)} =$$
$$(g^{j,(c)}[v])^3{}_{v=0} with \, g^{j,(c)}[v] =$$
$$\sum_{(x',y')\in I_v^{(c)}} \varphi_{I_v}^{(c)} [x',y'] g^{j-1}[x',y'] \qquad (13)$$

as well as the 3 high-pass parts for l will be assigned as1, 2, 3

$$s^{j,(c)} =$$
$$(s_l^{j,(c)}[v])^3{}_{v=0} with \, s_l^{j,(c)}[v] =$$
$$\sum_{(x',y')\in I_v^{(c)}} \psi_{I_v}^{(c)} [x',y'] g^{j-1}[x',y']$$
$$(14)$$

Because this data is needed at reconstructing time by saving the c(covering) for every block Q_(m,n) that is utilized for partitioning.

3. We use a reshape function R to reorder the vector entries g^(j,(c)) and S l^(j,(c)) into 2 × 2 matrices, allowing us to apply extra levels of the tetrolet decomposition process.

204

$$g^j_{l/Q_{m,n}} = Rg^{j,(c)} =$$
$$\begin{pmatrix} g^{j,(c)}[0] & g^{j,(c)}[1] \\ g^{j,(c)}[2] & g^{j,(c)}[3] \end{pmatrix}.$$
(15)

and in the same way

$$S^j_{l/Q_{m,n}} = R\left(S^{j,(c)}_l\right), l=1,2,3.$$
(16)

4. Getting the result of tetrolet decomposition in every block $Q_{m,n}$ $m, = 1...\frac{N}{2^{j+1}}$, then the low-pass matrix will be stored.

$$g^j = \left(g^j_{l/Q_{m.n}}\right)^{\frac{N}{2^{j+1}}}_{m,n=1}$$ & the high-

pass matrices $s^j = \left(s^j_{l/Q_{m.n}}\right)^{\frac{N}{2^{j+1}}}_{m,n=1}$

l=1,2,3, replacing the low-pass image $g^{j-1}$by the matrix$\begin{pmatrix} g^j & s^j_2 \\ s^j_1 & s^j_3 \end{pmatrix}.$ Thus, obtained 1 low-pass image (subband) **g**j and 3 high=pass subbands s^j_1, s^j_2 and s^j_3in the decomposition level j.

5. After we use a shrinking approach to the tetrolet parameters following an appropriate number of decomposition stages to produce a sparse picture representation.

6. Redesign the filter bank algorithms by applying the first step through the fourth step to low-pass pictures up to the necessary no. of decomposition layers.

3.4 Feature Selection

The selection of characteristics refers to the process of selecting a subset function from the database. By removing redundant, irrelevant, and noisy characteristics, feature

extraction can be described as an optimization problem to speed up computing and increase accuracy.

- **Harris Hawks Optimization**

The hunting strategies of Harris Hawks birds are imitated using a novel population-based optimization method known as Harris Hawks Optimization (HHO). It is gradient-free. Heidari et alintroduction .'s of HHO in 2019 is recent[18]. The program mimics the natural hunting tactics used by Harris hawks, such as prediction, predation, and surprise pounces. Figure 2 illustrates the discovery and exploitation stages of HHO, which are similar to those of other metaheuristic algorithms. HHO, on the other hand, has 4 components for exploitation and two phases for exploration. These phases are particularly characterized in the following way.

205
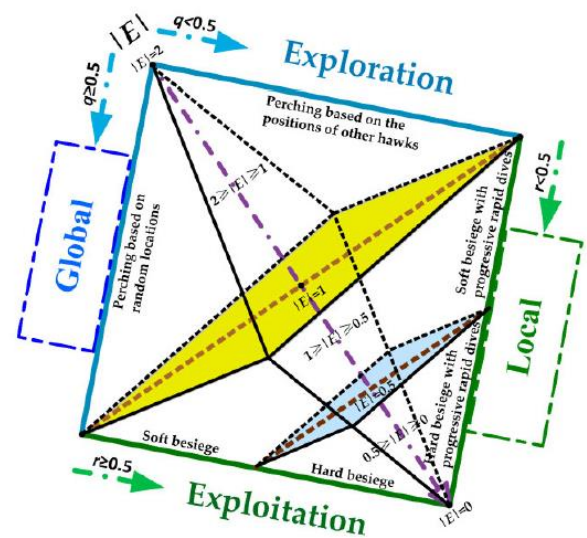
Figure 2. Exploration and exploitation phases of HHO

Initialization Phase: Resolution space and optimisation strategy have both been defined in this step. Additionally, the initial

population is made and the input parameters are supplied.

Exploration Phase: Harris Hawks is searching for a prey in this manner (a rabbit). Although the hawks' keen eyes can help them locate and keep a watch on their prey, it can occasionally be challenging to see the prey. The hawks in this situation are awaiting to monitor the location to see the prey. In reality, all Harris hawks are the potential answers for each repetition, and each one's fitness value is chosen based on the prey that it is meant to catch.

Exploitation Phase: Harris hawks are attacking the prey in this phase based on the location that was discovered in the previous stage. The hawks are still employing their chasing strategy, but the rabbit is still making an effort to escape. As a result, HHO is designed around four potential attack techniques. R demonstrate which approach should be used. While R denotes the rabbit's escape energy, r denotes the likelihood that the rabbit will succeed in escaping, with an r 0:5 for success and an r 0:5 for failure.

3.5 Classification

The act of categorizing involves grouping things into categories based on their kind and pattern. For diverse datasets, choosing the right classifier increased performance and accuracy. The cancers in this area are divided into benign and malignant tumors. To make the procedure more effective than the current process, the suggested system integrates a CNN classification algorithm. CNN contributes to improving the precision

in identifying the precise tumor-damaged region.

- **Proposed CNN Model for Multi-Class Brain Cancer Classification**

Kunihiko Fukushima developed CNNs in 1980 and Haner et al. modified them in 1998. The six different layer types that makeup CNN are input, convolutional, non-linear, pooling, totally connected, and output layers. The standard CNN design can be shown in Fig.-Fig. 1. One of the most striking methods for deep learning, Convolutional Neural Networks (CNNs), allows for the resilient growth of several layers of neurons. They have demonstrated an extraordinary capability of generalizing big data sets containing millions of images[19]. Computer vision-related activities that handle two-dimensional images are built in an intricate topology, which results in these outcomes. Regarding multi-channel colour images, additional metrics might be considered.
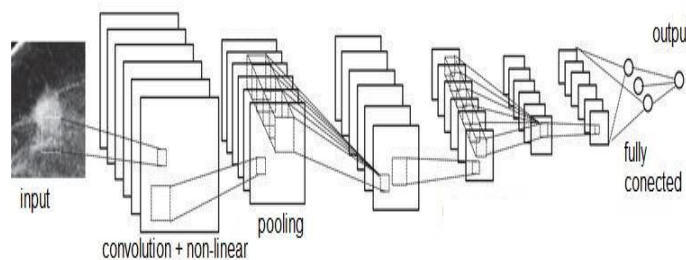
Fig. 1. Convolutional neural network.

A decent algorithm's gradient is used to optimize the loss function of a CNN trained on feedforward evaluation. The CNN format we used to represent brain cancer is not the typical CNN format [20–23].

By applying Volterra's theory, it is possible to enhance CNNs' capacity for learning and

206

adapting to the spatial domain. CNNs were previously employed to study non-linear physiological functions.

A 2nd order Volterra sequence for our proposed Convolution provided a patch on the input $I \in IR^{k_h \times k_w}$ with n elements (n=$k_h . k_w$), reshaped as a vector $X \in IR^n$:

$$X = [x_1 \ x_2 \dots x_n]^T \qquad (17)$$

A linear filter's input-output properties are as follows:

$$y(x) = \sum_{i=1}^{n}(w_1^i x_i) + b \qquad (18)$$

Where b is the bias and $w1i$ is the weights of the functional forms of the convolution obtained in a vector $w1$. Our method enables the quadratic version of this concept to be represented as follows:

$$y(x) = \sum_{i=1}^{n}(w_1^i x_i) + \sum_{i=1}^{n}\sum_{j=1}^{n}(w_2^{i,j} x_i x_j) + b \qquad (19)$$

Here, w_2^(i,j) denotes the weight of the filter's 2nd-order elements. An upper triangular form for the matrix w_2 with its weights is taken so that the no. of trainable variables for a 2nd order kernel is n(n + 1)=2 to avoid taking into account the terms of interaction twice for each pair of input components (x_i 〖; x〗_j). For a command r filter based on Volterra, the generic form for determining the total no. of parameters, n_v, is:

$$n_v = \frac{(n+r)!}{n! r!} \qquad (20)$$

$$y(x) = \underbrace{X^T w_2 X}_{quadratic\ term} + \underbrace{W_1^T X}_{linear\ term} + b \qquad (21)$$

While for the Volterra kernels we have the:

$$W2 = \begin{bmatrix} w_2^{1,1} & w_2^{1,2} & \cdots & w_2^{1,n} \\ 0 & w_2^{2,2} & \cdots & w_2^{2,n} \\ \vdots & & \ddots & \vdots \\ 0 & 0 & \cdots & w_2^{n,n} \end{bmatrix}$$

$$(22)$$

Containing the coefficients $w_2^{i;j}$ of the quadratic term, and:

$$w_1^T = [w_1^1 \ w_1^2 \dots w_1^n] \qquad (23)$$

including the linear term's coefficients w_1^i. The outcome of the suggested convolution can therefore be written as follows:

$$y(X) = \begin{bmatrix} w_2^{1,1} \\ w_2^{1,2} \\ w_2^{1,3} \\ . \\ . \\ . \\ w_2^{n,n} \end{bmatrix}^T \begin{bmatrix} x_1 x_1 \\ x_1 x_2 \\ x_1 x_3 \\ . \\ . \\ . \\ x_n x_n \end{bmatrix} + \begin{bmatrix} w_1^1 \\ w_1^2 \\ w_1^3 \\ . \\ . \\ . \\ w_1^n \end{bmatrix}^T \begin{bmatrix} x_1 \\ x_2 \\ x_3 \\ . \\ . \\ . \\ x_n \end{bmatrix} + b$$

$$(24)$$

Be aware that the weights w 2^(i;j) indicate a correlation to the spatial positions of the input elements x_i and x_j that interaction. Superscripts (i; j) are used to indicate this. Backpropagation can be described mathematically as follows:

$$\frac{\partial y}{\partial w_1^i} = x_i \qquad \frac{\partial y}{\partial w_2^{i,j}}$$
$$= x_i x_j \qquad (25)$$
$$\frac{\partial y}{\partial x_i} = w_1^i +$$
$$\sum_{k=1}^{i}(w_2^{k,i} x_k) + \sum_{k=1}^{n}(w_2^{i,k} x_k) \qquad (26)$$

4 PERFORMANCE METRICS

Sensitive, specificity, accuracy, precision, resemblance, and border error are the statistical measures. The per cent of the true lesion that has been recognized by

207

the automated approach is displayed in the next sentence. Table 4 displays the suggested technique's performance measures results. The suggested methodologies' performance metrics are contrasted with the current methodology, and the results are displayed in table 5.

$$\text{Jaccard Index} = J(P,G) = \frac{S(P \cap G)}{S(P \cup G)} \quad (27)$$

$$\text{Dice Overlap Index (DOI)} = D(P,G) = 2X \frac{P \cap G}{P+G} \quad (28)$$

$$\text{Similarity Index} SI = \frac{2X Truepositive}{2X truepositive + falsepositive + falsenegative} \quad (29)$$

$$\text{Absolute Volume Measurement Error (AVME)} = (\frac{V_{automatic}}{V_{manual}} - 1) \times 100\% \quad (30)$$

$$\text{Figure of Merit}(\varepsilon) = 1-(\varepsilon) = 1 - \frac{|V_{manual} - V_{automatic}|}{V_{manual}} \quad (31)$$

$$\text{Sensitivity} = \frac{TP1}{TP1 + FN1} \times 100\% \quad (32)$$

$$\text{Specificity} = \frac{TN1}{TN1 + FP1} \times 100\% \quad (33)$$

$$\text{Accuracy} = \frac{TP1 + TN1}{TP1 + FP1 + FN1 + TN1} \times 100\% \quad (34)$$

$$\text{Precision} = \frac{TP1}{TP1 + FP1} \times 100\% \quad (35)$$

$$Recall = \frac{TP}{TP + FN} \times 100 \quad (36)$$

$$F - measure = \frac{2*Precision*Recall}{Pr ecision + Recall} \quad (37)$$

Where,

TN is True Negative

TP is True Positive

FP is False positive

FN is False negative

5. EXPERIMENTAL RESULTS

- **Data sets**

To evaluate our image categorization algorithm's performance, we used three benchmark data sets. The initial is called DICOM Data Gathering, which stands for Digital Imaging and Communications in Medicine. 22 images of brain tumors are included in DICOM. Both DICOM pictures have the DCM extension and are encoded using the JPEG2000 transmission syntax. The contained images don't have any ground-based representations of reality. Brain Web Data Set[35] is the second data source that has been compiled. Includes information from simulated brain MRIs based on anatomical models for both healthy and Multiple Sclerosis (MS). To reproduce complete 3-dimensional data volumes, three series (T1-, T2-, and Proton Density-(PD-) weighted) were used, each with a different slice thickness, amount of noise, and strength non-uniformity. Files in this data collection have the "MNC" extension. Its T1 mode has a 1 mm slice thickness, 20% RF non-uniformity strength, and 3% noise (determined based on the

208

tissue that is brightest). There are 152 images in this dataset.

Simulation Outputs

In the steps that follow, the results of using the initial brain MRI image from the database are displayed. Preprocessing techniques are used to enhance the clarity of the images and minimize noise (2-4).

Following this, the tumor area from the images is segmented, as seen in Figure 5. The resultant characteristics are taken from the segmentation results in Table 3 and reduced. To reach a better level of intensity and accuracy, the classification method is then used.

(a)   (b)

(a)   **(b)**
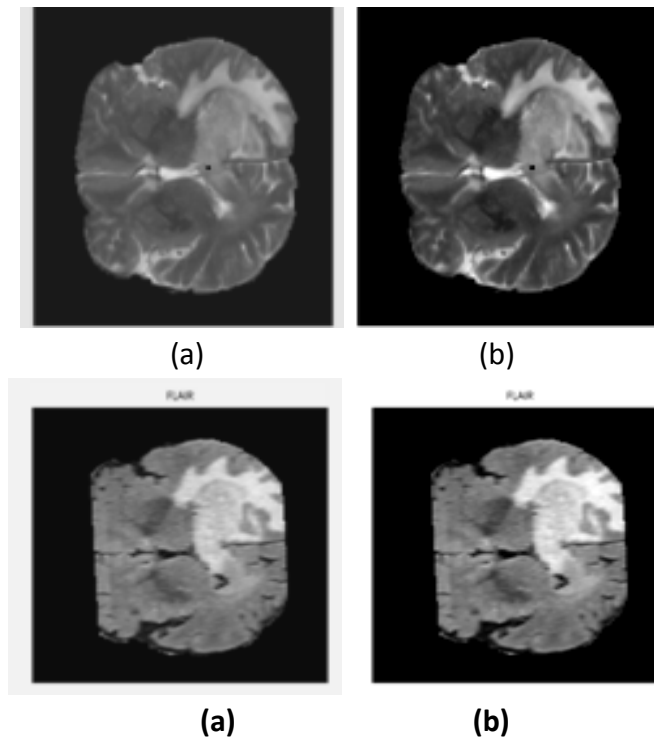
Figure 3: Preprocessed results of MRI images

(a)
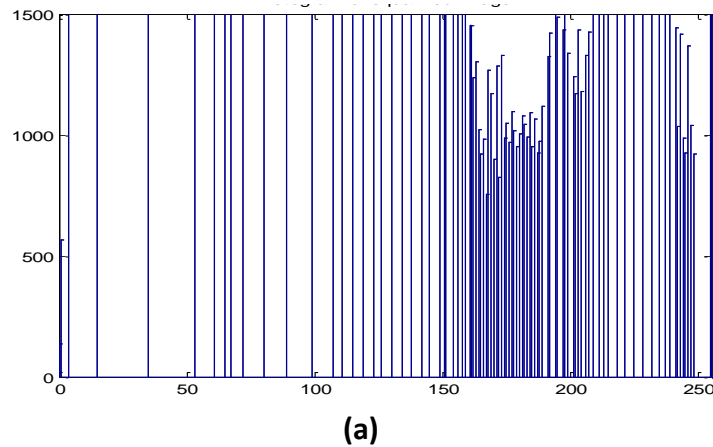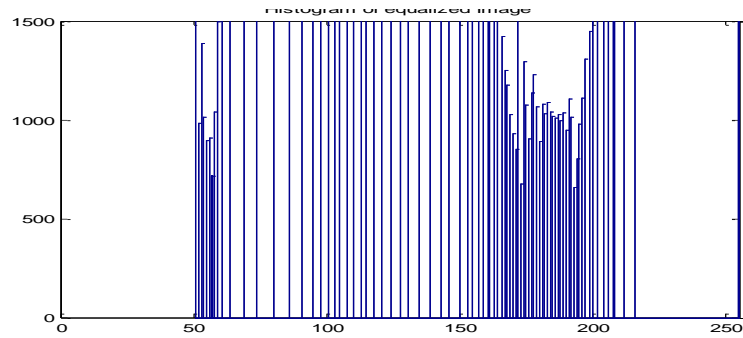
(b)

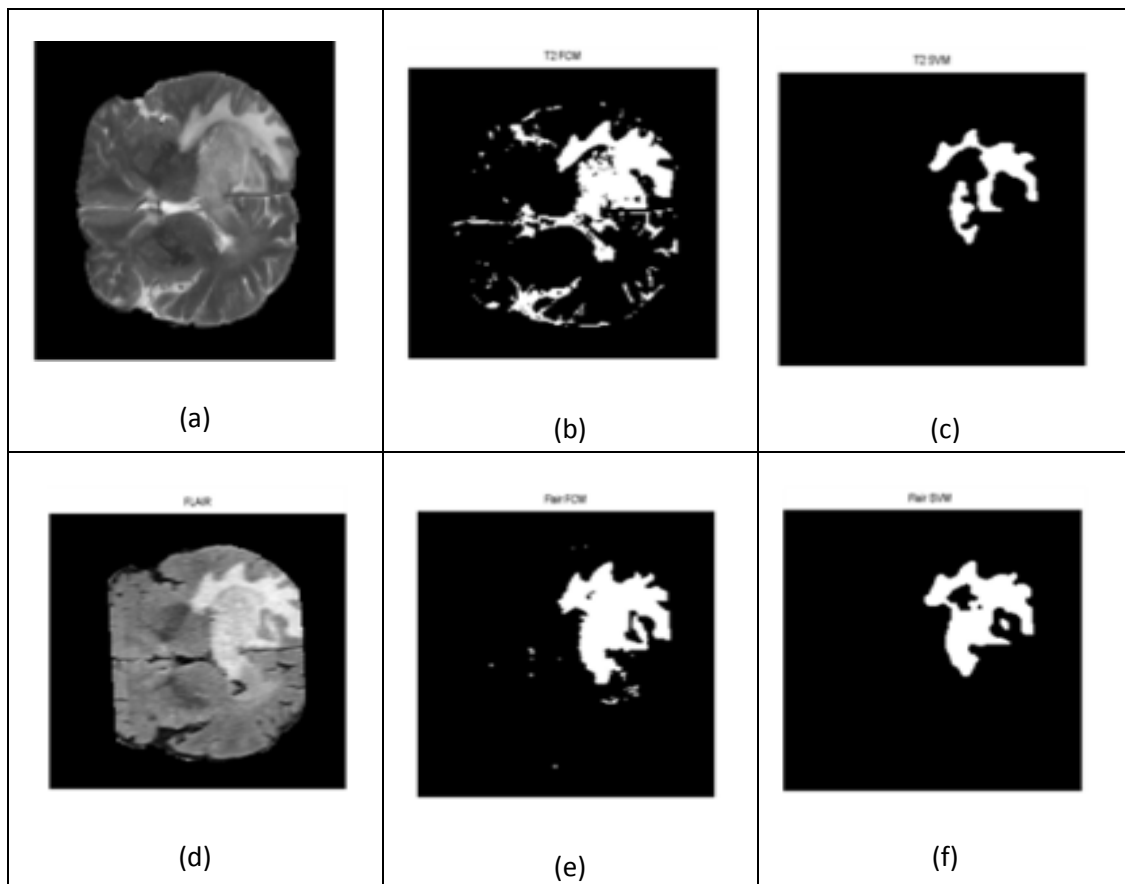**Figure 4: Histogram plot results of MRI images**

Figure 5: (a) & (d) input MRI image, (b) & (e) final hybrid deformable model with fuzzy method, (c) & (f) Final super pixel based adaptive clustering method segmented output

The absolute volume standard errors, figures of merit, Jaccard index, dice coefficients, and spatial overlap are some of the assessment matrices that were used to gauge the effectiveness of segments. Tables 1 and 2 display the segmented ROI volume measurements and associated ground truth values. The average Dice coefficient and Jaccard index that were determined are both 0.79. Both numbers indicate increased efficiency compared to the hybrid deformable

model with a fuzzy approach. With an average of 0.77, the AVME has improved and decreased the merit value number. The average spatial overlap is 0.91, and the majority of studies demonstrate that superpixel-based adaptive clustering outperforms hybrid deformable models using a fuzzy approach in terms of performance. The outcomes of the main classification produced by fusing a hybrid deformable model with a fuzzy technique are shown in Table 1.

IMAGES	DICE COEFFICIENT	JACCARD INDEX	ABSOLUTE VOLUME MEASUREMENT ERROR	FIGURE OF MERIT	SPATIAL OVERLAP
1	0.81	0.8	24.49	0.83	0.89
2	0.84	0.72	-28.49	0.6	0.83
3	0.82	0.86	-18.6	0.71	0.9
4	0.61	0.78	-22.13	0.91	0.88
5	0.63	0.92	-7.88	0.75	0.96
6	0.75	0.78	28.86	0.77	0.87
7	0.87	0.83	20.13	0.81	0.91
8	0.85	0.61	-39.22	0.71	0.76
9	0.75	0.87	-13.31	0.81	0.93
10	0.77	0.83	-16.89	0.81	0.91

Table 2: The outcome of superpixel-based adaptive clustering according to several evaluation matrices

Images	Dice Coefficient	Jaccard Index	Absolute Volume Measurement Error (AVME)	Figure of merit (FoM)	Spatial overlap
1	0.84	0.87	14.25	0.83	0.93
2	0.79	0.87	-13.01	0.6	0.93
3	0.91	0.84	-14.92	0.71	0.91
4	0.88	0.76	-23.63	0.91	0.87
5	0.52	0.98	1.55	0.75	0.99
6	0.84	0.81	22.99	0.77	0.9
7	0.8	0.76	32.21	0.81	0.86
8	0.71	0.77	-22.79	0.71	0.87
9	0.9	0.96	-4.44	0.81	0.98
10	0.78	0.83	20.81	0.81	0.91

According to Table 4, the image's True Positive scores should always be greater for better results, and its False Negative numbers should be as low as feasible. The outcome of the

experiment shows that compared to conventional classifiers, utilizing a deep learning classifier results in a high level of overall accuracy. Our tests on several images show that the suggested strategy performs effectively in both situations where the image's objects are difficult to distinguish from the backdrop and when they are distinct from it.

Figures 6 and 7 demonstrate how well the CNN classifier performs and how accurate it is. 5 phases with convolution and an Identification block make up this CNN ResNet-50 model. Each convolution block consists of three convolution layers, whereas each identification block consists of three convolution operations. The training information set for the ResNet-50 consists of about 23 million elements. The First Sections of the Convolution Layer and Resnet Weights are shown in the figure. CNN has a 98.3% average accuracy rate. The recommended accuracy contrasts with the cutting-edge approaches depicted in Figure 8 in terms of accuracy.

Table 4:Values from the Classifier are compared with those from the confusion matrix.

Classifier	TP (%)	FP (%)	FN (%)	TN (%)
SVM	41.9	57.7	42.3	58.1
Back propagation	45.6	56.1	43.9	54.4
ANN	44.9	56.6	43.4	55.1
CNN	48.5	64.9	35.1	51.5

Table 3: Feature extraction result

Image No	GLCM Feature				First Order Statistics(FOS) Feature				
	Contrast	Correlation	Energy	Homogeneity	Mean	Standard Deviation	Skewness	Kurtosis	Entropy
1	0.00856	0.9774	0.612	0.9957	0.0060	0.0108	2.017	5.7602	2.385
2	0.00558	0.96863	0.816	0.9972	0.0130	0.0189	1.3844	3.3770	2.9833
3	0.00533	0.97829	0.748	0.9973	0.0090	0.0127	1.6556	4.7305	2.7723
4	0.00521	0.97631	0.774	0.9973	0.0110	0.0132	1.2441	3.3380	2.9128
5	0.00664	0.97336	0.743	0.9966	0.0110	0.0191	2.2741	7.1078	2.6871
6	0.00572	0.98352	0.646	0.9971	0.0060	0.0103	1.6051	4.2824	2.0535
7	0.00875	0.95669	0.789	0.9956	0.0080	0.0107	1.5780	4.1386	2.5775

8	0.00459	0.96922	0.846	0.9977	0.0100	0.012	0.8265	2.4777	2.7748
9	0.00962	0.97687	0.574	0.9951	0.0110	0.014	0.9457	2.6559	2.2390
10	0.0074	0.98272	0.559	0.9962	0.0100	0.0081	0.4199	2.2836	2.8144
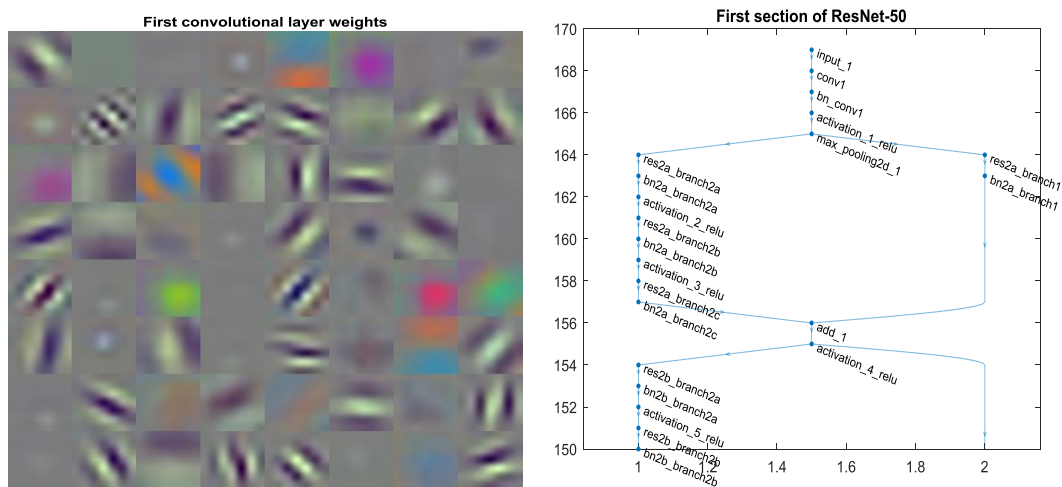
Figure 6: The First Convolution Layer Weights and First Section of Resnet

Figure 7: Confusion matrix of proposed CNN

Table 4: Performance value of CNN

classifier	CNN
Accuracy (%)	98.3
Error (%)	1.7
Sensitivity (%)	97.9
Specificity (%)	98.62
Precision (%)	96.83
F1_score	0.9521

Table 5: Comparison of accuracy in different classifiers

Number of test images (normal = 50, abnormal = 50)				
Evaluation parameter	SVM	Back Propagation	K-NN	Proposed classifier (CNN)
Specificity (%)	91.74	92.54	94.72	98.62
Sensitivity (%)	96.2	97.2	97.5	97.9
Accuracy (%)	90.03	95.46	96.51	98.3
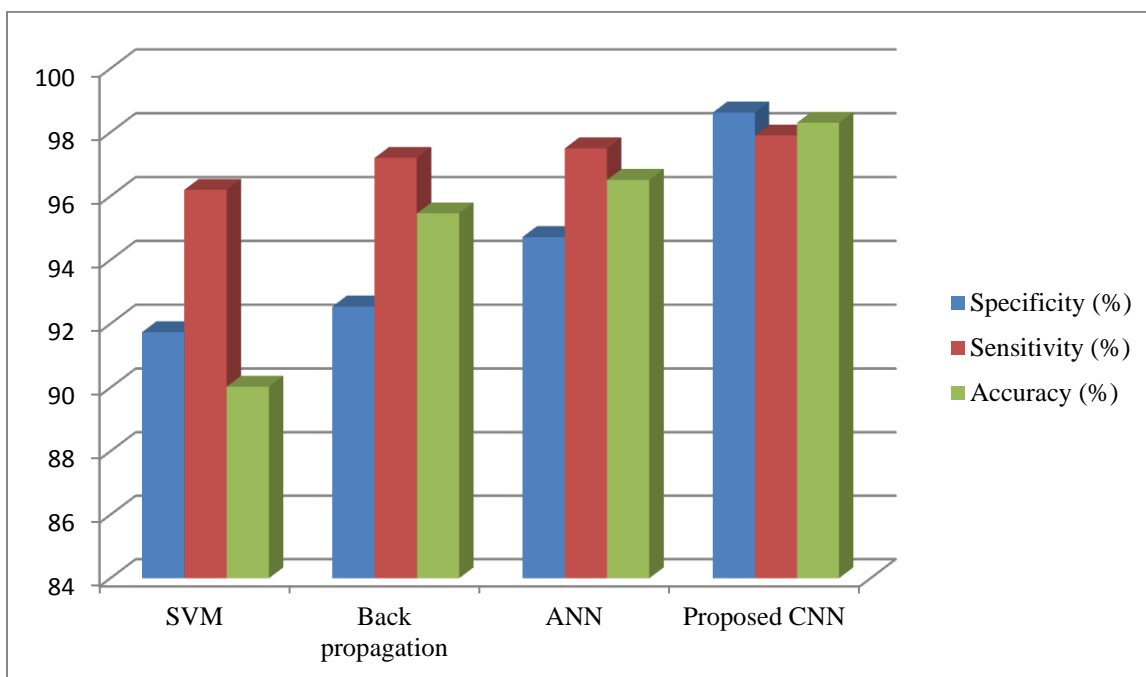
Figure 8: Comparison plot of various classifiers

The proposed Classifiers are compared with the different classifiers in the ROC Curve. The technique works better than the alternative approach for a brief analysis of the malignant zone, as indicated by the high True Positive result.
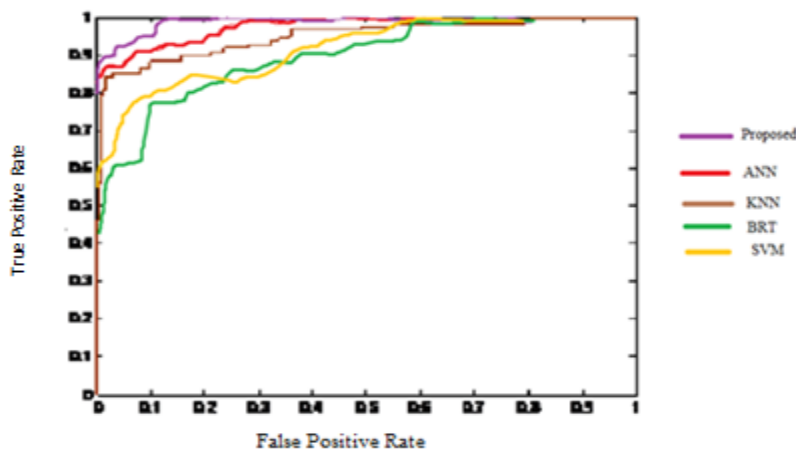
Fig 9. ROC curve for Deep Learning Classifier

Creating an effective automated process for fragmenting brain tumors by dividing them into normal and abnormal classifications is the main goal of the current research. The use of CNN methods, which are well-liked and efficient segmentation and classification methods, will be very advantageous for image analysis. These techniques can also be used to section and classify a variety of neurological disorders, including Parkinson's disease, Alzheimer's disease, stroke, and autism.

6. CONCLUSION

Deep Convolutional Neural Networks (CNNs) are increasingly being used in both the corporate and scientific worlds for classification. In this research, the effectiveness of a deep learning model was examined for a classification issue involving the identification of brain tumors. The ResNet model update shows the exceptional performance that the deep learning model used in natural image analysis is competent while evaluating medical images. Using an MRI of the brain, the suggested method was developed to detect brain cancers. To remove noise and identify the tumor component in a brain image, a unique boosted adaptive anisotrophic diffusion filter is utilized in many stages. By segmenting, the tumor component is removed. The suggested system makes use of textural feature extraction. The proposed system's classification accuracy was 98.3% using CNN classifiers. The use of intricate perfusion-based MRI pictures is a future improvement.

References

1. Saba, Tanzila, Ahmed Sameh Mohamed, Mohammad El-Affendi, Javeria Amin, and Muhammad Sharif. "Brain tumor detection using the fusion of handcrafted and deep learning features." Cognitive Systems Research 59 (2020): 221-230.

2. Sharif, Muhammad, Javaria Amin, Muhammad Wasif Nisar, Muhammad Almas Anjum, Nazeer Muhammad, and Shafqat Ali Shad. "A unified patch-based method for brain tumor detection using features fusion." Cognitive Systems Research 59 (2020): 273-286.

3. Toğaçar, Mesut, Burhan Ergen, and Zafer Cömert. "BrainMRNet: Brain tumor detection using magnetic resonance images with a novel convolutional neural network model." Medical Hypotheses 134 (2020): 109531.

4. A.Veeramuthu, S.Meenakshi, V. Priya Darsini 'Brain Image Classification using Learning Machine Approach and Brain Structure Analysis'2nd International Symposium on Big Data and Cloud Computing (ISBCC'15). Procedia Computer Science 50 (2015) 388 – 394. Available online at www.sciencedirect.com

5. Sanjeev Kumar, Chetna Dabas, Sunila Godara 'Classification of Brain MRI Tumor Images: A Hybrid approach' Information Technology

and Quantitative Management (ITQM2017. Procedia Computer Science 122 (2017) 510–517. Available online at www.sciencedirect.com

6. Gopal Chandra Jan, Aleena Swetapadm, Prasant Kumar Pattnaik 'Enhancing the performance of motor imagery classification to design a robust brain-computer interface using feed-forward back-propagation neural network' Ain Shams Engineering Journal 9 (2018) 2871–2878. Available online at www.sciencedirect.com

7. Sidhu, Harbir S., Salvatore Benigno, Balaji Ganeshan, Nikos Dikaios, Edward W. Johnston, Clare Allen, Alex Kirkham et al. "Textural analysis of multiparametric MRI detects transition zone prostate cancer." European radiology 27, no. 6 (2017): 2348-2358.

8. Anaraki, Amin Kabir, Moosa Ayati, and Foad Kazemi. "Magnetic resonance imaging-based brain tumor grades classification and grading via convolutional neural networks and genetic algorithms." Biocybernetics and Biomedical Engineering 39, no. 1 (2019): 63-74.

9. Fabelo, Himar, Samuel Ortega, Raquel Lazcano, Daniel Madroñal, Gustavo M Callicó, Eduardo Juárez, Rubén Salvador et al. "An intraoperative visualization system using hyperspectral imaging to aid in brain tumor delineation." Sensors 18, no. 2 (2018): 430.

10. Zhang, Jiachi, Xiaolei Shen, Tianqi Zhuo, and Hong Zhou. "Brain tumor segmentation based on refined fully convolutional neural networks with a hierarchical dice loss." arXiv preprint arXiv:1712.09093 (2017).

11. Wang, Na, Yu Shang, Yang Chen, Min Yang, Quan Zhang, Yi Liu, and Zhiguo Gui. "A hybrid model for image denoising combining modified isotropic diffusion model and modified Perona-Malik model." IEEE Access 6 (2018): 33568-33582.

12. Chang, Yakun, Cheolkon Jung, Peng Ke, Hyoseob Song, and Jungmee Hwang. "Automatic contrast-limited adaptive histogram equalization with dual gamma correction." IEEE Access 6 (2018): 11782-11792.

13. Haleem, Muhammad Salman, Liangxiu Han, Jano van Hemert, Baihua Li, Alan Fleming, Louis R. Pasquale, and Brian J. Song. "A novel adaptive deformable model for automated optic disc and cup segmentation to aid glaucoma diagnosis." Journal of medical systems 42, no. 1 (2018): 20.

14. Wang, Yueying, Hamid Reza Karimi, Hao Shen, Zhijun Fang, and Mingxin Liu. "Fuzzy-model-based sliding mode control of nonlinear descriptor systems." IEEE transactions on cybernetics 49, no. 9 (2018): 3409-3419.

15. Uziel, Roy, Meitar Ronen, and Oren Freifeld. "Bayesian Adaptive Superpixel Segmentation." In Proceedings of the IEEE International Conference on Computer Vision, pp. 8470-8479. 2019.

16. Pradhan, Jitesh, Sumit Kumar, Arup Kumar Pal, and Haider Banka. "A hierarchical CBIR framework using adaptive tetrolet transform and novel histograms from colour and shape features." Digital Signal Processing 82 (2018): 258-281.

17. Yang, Fei, Nesrin Dogan, Radka Stoyanova, and John Chetley Ford. "Evaluation of radiomic texture feature error due to MRI acquisition and reconstruction: a simulation study utilizing ground truth." Physica Medica 50 (2018): 26-36.

18. Sihwail, Rami, Khairuddin Omar, Khairul Akram Zainol Ariffin, and Mohammad Tubishat. "Improved Harris Hawks Optimization Using Elite Opposition-Based Learning and Novel Search Mechanism for Feature Selection." IEEE Access 8 (2020): 121127-121145.

19. Chuang, Tzu-Yi, Jen-Yu Han, Deng-Jie Jhan, and Ming-Der Yang. "Geometric Recognition of Moving Objects in Monocular Rotating Imagery Using Faster R-CNN." Remote Sensing 12, no. 12 (2020): 1908.

20. Ćiprijanović, Aleksandra, G. F. Snyder, Brian Nord, and Joshua EG Peek. "DeepMerge: Classifying high-redshift merging galaxies with deep neural networks." Astronomy and Computing 32 (2020): 100390.

21. Sarhan, Ahmad M. "Detection and Classification of Brain Tumor in MRI Images Using Wavelet Transform and Convolutional Neural Network." Journal of Advances in Medicine and Medical Research (2020): 15-26.

22. Singh, Satya P., Lipo Wang, Sukrit Gupta, Haveesh Goli, Parasuraman Padmanabhan, and Balázs Gulyás. "3D Deep Learning on Medical Images: A Review." arXiv preprint arXiv:2004.00218 (2020).

23. Chaubey, Nirbhay Kumar, and Prisilla Jayanthi. "Disease Diagnosis and Treatment Using Deep Learning Algorithms for the Healthcare System." In Applications of Deep Learning and Big IoT on Personalized Healthcare Services, pp. 99-114. IGI Global, 2020.

24. Joseph, Teena, S. A. Kalaiselvan, S. U. Aswathy, R. Radhakrishnan, and A. R. Shamna. "A multimodal biometric authentication scheme based on feature fusion for improving security in a cloud environment." Journal of Ambient Intelligence and Humanized Computing (2020): 1-9.

25. Aswathy, S. U., G. Glan Devadhas, and S. S. Kumar. "A tumour segmentation approach from FLAIR MRI brain images using SVM and

genetic   algorithm." International Journal of Biomedical Engineering and Technology 33, no. 4 (2020): 386-397.